# Experimental–numerical study on strain and stress partitioning in bainitic steels with martensite–austenite constituents

Noriki Fujita[a,*], Nobuyuki Ishikawa[a], Franz Roters[b], Cemal Cem Tasan[c], Dierk Raabe[b]

[a] *JFE Steel Corporation, Steel Research Laboratory, Japan*
[b] *Max-Planck-Institut für Eisenforschung, Germany*
[c] *Massachusetts Institute of Technology, Department of Materials Science and Engineering, USA*

ABSTRACT

To achieve safety and reliability in pipelines installed in seismic and permafrost regions, it is necessary to use linepipe materials with high strength and ductility. The introduction of dual-phase steels, e.g., with a bainite and dispersed martensite–austenite (MA) constituent, would provide the necessary ingredients for the improvement of the strain capacity (as required by a new strain-based linepipe design approach) and toughness. To fine-tune the alloy design and ensure these dual-phase steels have the required mechanical properties, an understanding of the governing deformation micromechanisms is essential. For this purpose, a recently developed joint numerical–experimental approach that involves the integrated use of microscopic digital image correlation analysis, electron backscatter diffraction, and multiphysics crystal plasticity simulations with a spectral solver was employed in this study. The local strain and stress evolution and microstructure maps of representative microstructural patches were captured with a high spatial resolution using this approach. A comparison of these maps provides new insights into the deformation mechanism in dual-phase microstructures, especially regarding the influence of the bainite and MA grain size and the MA distribution on the strain localization behavior.

## 1. Introduction

Recently, demand for greater efficiency in the transportation of oil and gas has driven the use of thinner but stronger linepipe steel for large-diameter pipelines. Furthermore, the reliability required for pipelines installed in seismic and permafrost regions necessitates high ductility and toughness. Therefore, the strain-based design approach has gained increasing acceptance in recent years, as this approach ensures high deformability to cope with the aggressive mechanical and thermal loads that act on pipelines constructed in such environments (Zhou et al., 2006). The deformability of linepipe steels in the strain-based design approach is parameterized by the yield-to-tensile strength ratio (Y/T), the strain hardening coefficient (n-value), and the uniform elongation (uEl). Generally, a low Y/T is desirable for linepipe steel and can be achieved in dual-phase microstructures containing both a high-strength phase (for high tensile strength) and a low-strength phase (for early yielding). These design constraints have lead to the use of ferrite–bainite pipeline steels (Ishikawa et al., 2005) because ferrite–martensite automotive steels (Calcagnotto et al., 2011; Kadkhodapour et al., 2011; Tasan et al., 2015) lack adequate low-temperature toughness. More recently, steels composed of bainite and martensite–austenite (MA) have been developed by applying an online heat treatment process in plate manufacturing (Shinmiya et al., 2008; Fan et al., 2014). During this treatment, deformed austenite (refined by controlled rolling) transforms partially into bainite after accelerated

cooling. In the retained austenite islands, only partial martensitic transformation is observed as a result of carbon enrichment from the transforming bainite phase, creating a nano-dual-phase MA island structure (Morooka et al., 2012).

In dual-phase steels, damage-induced local softening may cause early failure when the volume fraction, phase distribution, grain size, and hardness of the phases are not optimized (Calcagnotto et al., 2010; Han et al., 2013; Gioacchino and Clegg, 2014; Minami et al., 2012; Morooka et al., 2012). However, deformation mechanisms governing the material properties of the bainite-MA steels have not been fully clarified. A few existing reports have discussed overall toughness. For example, Shinmiya et al. (2008) observed that finely dispersed MA islands do not affect the toughness of bainite–MA steels, whereas coarse MA islands observed in the heat affected zone are considered to reduce toughness (Ishikawa et al., 2006; Lan et al., 2014; Li et al., 2017).

To fill this gap in our understanding, in the present study, the local deformation behavior in bainite–MA dual-phase steel was investigated through a coupled experimental–numerical approach. The methodology employed here combines in-situ scanning electron microscopy (SEM) deformation experiments, microscopic digital image correlation (μ-DIC) analysis, electron backscatter diffraction (EBSD) analysis, and crystal plasticity (CP) simulations with a spectral solver to provide information on the local microstructure and strain and stress evolution of complex microstructured alloys (Tasan et al., 2014a, 2014b; Yan et al., 2015; Bertin et al., 2016; Guery et al., 2016; Guan et al., 2017). These techniques allow the examination of the effect of grain orientation, phase boundaries, and microstructural morphology on the strain localization of multi-phase steel. The heterogeneous plastic micromechanical deformation in bainite–MA steel used for linepipe was quantitatively investigated to evaluate its work hardenability with the ultimate goal of optimizing its mechanical response.

## 2. Methodology

### 2.1. Materials

The microstructure of grade X70 and X80 linepipe was investigated. Steel slabs with chemical compositions containing 0.06C–0.15Si–1.8Mn were produced in a laboratory vacuum furnace and cast into 150 kg ingots. Online heat treatment was applied to create the bainite–MA microstructure, as shown in Fig. 1. The ingots were reheated at 1150 °C and then hot rolled to 22 mm thick plates. The slab temperature was measured by inserting a thermocouple at the plate center at the midpoint in the thickness direction. Controlled rolling was applied at a temperature below the non-recrystallization temperature $T_{nr}$. Accelerated cooling of the plate was then performed from a temperature of 993 K, which is below the ferrite formation temperature $A_{r3}$, and stopped at a temperature of 773 K. An austenite microstructure refined by controlled multipass rolling initiated the bainite transformation during accelerated cooling. The microstructure after accelerated cooling was a composite consisting of bainite and untransformed austenite. Subsequent online heating to a temperature of 873 K, which is below $A_{c1}$, was applied after accelerated cooling. After online heating, the microstructure was air cooled to room temperature. The dislocation density in the bainite matrix decreased during subsequent online heating, and the supersaturated carbon contained in the bainite matrix became concentrated in the untransformed austenite. This tempering process softens the bainite matrix. However, untransformed austenite with supersaturated carbon is partially transformed into fine and isometric martensite during air cooling. Retained austenite is typically softer than other austenite phases, but the retained austenite in bainite–MA steel showed a carbon concentration about 10 times higher than the matrix (Ishikawa et al., 2014) and an intermediate hardness between those of bainite and martensite because of the presence of supersaturated carbon (Takahashi et al., 2012).

For the experiments, tensile specimens with gauge dimensions of 20 mm × 5 mm × 1 mm were cut parallel to the rolling direction from the plate center at the midpoint in the thickness direction. Table 1 gives the mechanical properties of the bainite–MA steel. The specimen surfaces were prepared using a conventional metallographic grinding and diamond polishing approach and finished with colloidal $SiO_2$ polishing. The microstructure was etched by nital and electrolytic etching. Fig. 2 shows SEM micrographs of the microstructure and the stress–strain curve obtained from the tensile test. In this figure, the black and red flow curves correspond to the curves obtained from the tensile test of the bainite–MA dual-phase steel and the stress–strain data used in the CP simulation, respectively. Details of the decomposition of the flow curves into the curves describing the individual phases will be
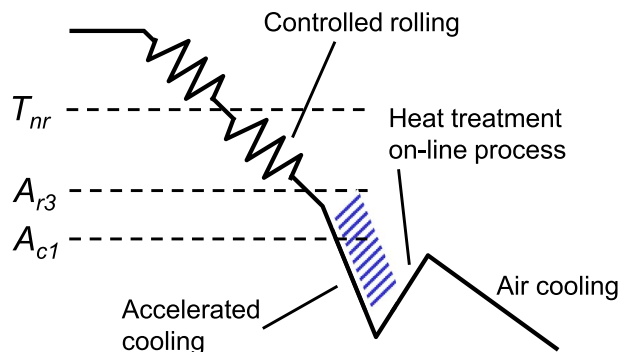


**Fig. 1.** Schematic of the rolling and heat treatment processes conducted at a laboratory scale.

**Table 1**
Mechanical properties of the steel used in this study.

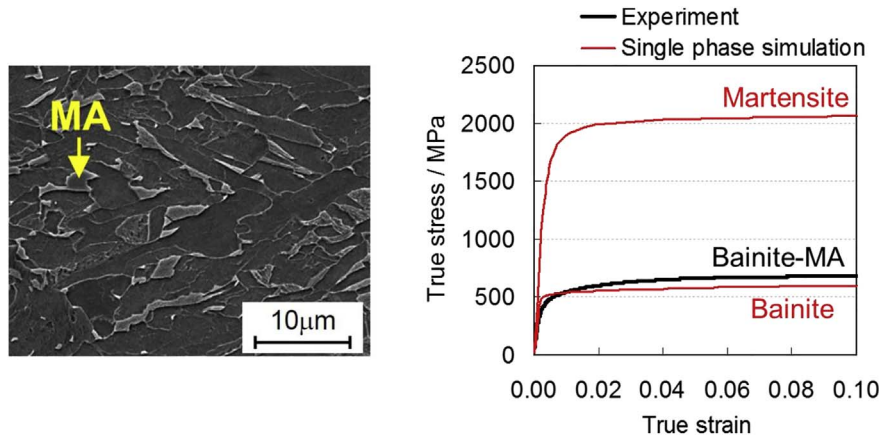| YS [MPa] | TS [MPa] | uEl [%] | EL [%] |
|---|---|---|---|
| 505 | 706 | 7.6 | 24 |



**Fig. 2.** SEM micrograph and stress–strain curves of the bainite–MA steel used in this study.

explained in the next section. Table 2 shows the measurement results for the material microstructure. The phase volume fraction and grain size were calculated from several EBSD measurement areas using orientation imaging microscopy (OIM) analysis software (OIM Analysis 7.0, EDAX/TSL), as described in a later section.

## 2.2. Experimental strain mapping

In this study, the specimens were prepared using an approach by Yan et al. (2015), in which colloidal $SiO_2$ for DIC patterning is dispersed on the surface of a tensile specimen after polishing. In comparison with conventional patterning techniques, this approach is advantageous in that it can be used in combination with local strain analysis and microstructure analysis without mutual signal interference (Tasan et al., 2010; Minami et al., 2012).

Information on the microstructure of the bainite–MA steel before deformation was evaluated by EBSD. EBSD measurements were carried out using a scanning electron microscope (JSM-6500F, JEOL). An acceleration voltage of 15 kV with a step size of 30 nm was chosen for the EBSD measurements. The EBSD data were used to create the model for the CP simulation.

In-lens secondary electron (SE) images were recorded to acquire the distribution pattern of colloidal $SiO_2$ in the EBSD measurement area. These images were obtained with a focused ion beam (FIB) scanning electron microscope (1540 XB Crossbeam, Zeiss). The in-lens detector was placed in the electron beamline and is highly sensitive to specimen surface conditions (e.g., contamination, charging, and oxidation). Therefore, colloidal $SiO_2$ on the surface of a specimen was easily visualized. A low acceleration voltage of 1.5 kV with a small aperture was chosen to obtain high-resolution (3072 × 2304 pixels) in-lens SE images. Back-scattered electron (BSE) images were also recorded to observe the grain shape and match the coordinates of the in-lens SE images and the EBSD maps.

The tensile specimens were deformed at a strain rate of $2.5 \times 10^{-4} \, s^{-1}$ up to a total strain of 0.11. At each deformation level, the microstructure was imaged using different SEM detectors (SE, BSE, in-lens SE, and EBSD detectors). The images captured by the in-lens SE detectors were used for DIC analysis (ARAMIS 6.3 software; Sachtleber et al., 2002; Raabe et al., 2003). The strain maps in DIC can be visualized over the entire observation area by selecting a suitable subset area and spacing according to the conditions of the colloidal $SiO_2$ distribution. In this study, the resolution of the strain measurement was approximately 100 nm, which enabled the measurement of the local strain around fine MA islands.

## 2.3. Crystal plasticity simulation

CP analysis was used for the numerical simulation of the high-resolution strain mapping data obtained by DIC analysis. The same

**Table 2**
Average microstructure characteristics of the steel used in this study.

| MA volume fraction [%] | Bainite grain size [μm] | MA grain size [μm] |
|---|---|---|
| 2.65 ± 1.77 | 6.00 ± 1.95 | 1.00 ± 0.25 |

EBSD information as in the DIC analysis was used to define the initial conditions for the CP analysis (Raabe et al., 2001; Zhao et al., 2008). The CP analysis technique is based on the assumption that plastic deformation proceeds along specific shear vectors on certain slip planes (Roters et al., 2010). The DAMASK (the Düsseldorf advanced material simulation kit) framework (Roters et al., 2012) was used for the CP analysis in this work. This integrated framework enables CP simulations in conjunction with various types of constitutive models. The major constitutive formulations are a viscoplastic phenomenological model (Peirce et al., 1982), a dislocation-based model incorporating twinning-induced plasticity (TWIP) effects (Roters et al., 2000; Steinmetz et al., 2013), and a formulation that considers dislocation fluxes (Reuber et al., 2014). In this study, the phenomenological model was employed because the constitutive parameters for this model can be estimated from actual macroscopic deformation behavior.

The plastic strain $L_p$ in the CP simulations is represented as the summation of the shear slip in slip systems:

$$L_p = \sum_{\alpha=1}^{24} \dot{\gamma}^\alpha (\mathbf{b}^\alpha \otimes \mathbf{n}^\alpha) \tag{1}$$

where $\dot{\gamma}$ is the shear strain rate and the superscript $\alpha$ (= 1, 2, …, 24) is the slip system index. The vectors $\mathbf{b}^\alpha$ and $\mathbf{n}^\alpha$ are unit vectors describing the slip direction and the normal to the slip plane, respectively. The body-centered cubic crystal structure with $< 111 > \{110\}$ and $< 111 > \{112\}$ slip system families was applied for each phase (Raabe, 1995a, 1995b). The strain rate in each slip system is given by the following rate-dependent model:

$$\dot{\gamma}^\alpha = \dot{\gamma}_0 \left| \frac{\tau^\alpha}{S^\alpha} \right|^n \text{sgn}(\tau^\alpha) \tag{2}$$

where $\dot{\gamma}_0$ is the reference shear strain rate, $\tau^\alpha$ is the resolved shear stress on the $\alpha^{\text{th}}$ slip system, and $S^\alpha$ is the slip resistance in the $\alpha^{\text{th}}$ slip system. $n$ is a strain rate exponent. The hardening is given by

$$\dot{S}^\alpha = \sum_{\alpha=1}^{24} \dot{\gamma}^\alpha h_0 \left| 1 - \frac{S^\alpha}{S_\infty^\alpha} \right|^w \text{sgn}\left( 1 - \frac{S^\alpha}{S_\infty^\alpha} \right) h_{\alpha\beta} \tag{3}$$

where $S_\infty$ is the saturation slip resistance, $h_0$ is the initial hardening rate, $h_{\alpha\beta}$ is the interaction parameter, and $w$ is a fitting parameter.

To express the ductile damage nucleation after plastic deformation around the bainite matrix, an isotropic ductile damage model was coupled with the CP analysis.

The deformation gradient $\mathbf{F}$ can be expressed in a multiplicative decomposition, as

$$\mathbf{F} = \mathbf{F}_e \mathbf{F}_p \tag{4}$$

The effective elastic stiffness $\mathbb{C}_{eff}$ relates the elastic deformation gradient $\mathbf{F}_e$ to the second Piola-Kirchhoff stress, as

$$\mathbf{S} = \frac{1}{2} \mathbb{C}_{eff} : (\mathbf{F}_e^T \mathbf{F}_e - \mathbf{I}) \tag{5}$$

The effective elastic stiffness can be defined from the stiffness tensor $\mathbb{C}$ degraded by the non-local damage $\phi_{nl}$, as

$$\mathbb{C}_{eff} = \phi_{nl}^2 \mathbb{C} \tag{6}$$

Damage localization was avoided by introducing a gradient term in the damage regularization equation, as

$$M\dot{\phi}_{nl} = l^2 \nabla \cdot \mathbf{D} \cdot \nabla \phi_{nl} + (\phi_l - \phi_{nl}) \tag{7}$$

where $M$ is the mobility, $\phi_{nl}$ is the phase field parameter, $\phi_l$ is the local damage, $l$ is the length scale, and $\mathbf{D}$ is the second-order diffusion tensor. When $\phi_{nl}$ takes a value of 1 or 0 at a material point, this indicates that the material is undamaged or totally damaged, respectively.

Ductile damage mainly proceeds by the nucleation, growth, and coalescence of voids. These three processes are largely driven by the accumulation of local plastic deformation and stress triaxiality. If the effects of stress triaxiality contributing to the ductile damage propagation are neglected, the local damage can be defined as

$$\phi_l = \min \left( 1, \frac{(\phi_{nl})^m \gamma_{crit}}{\sum_{\alpha=1}^{24} \gamma^\alpha} \right) \tag{8}$$

where $\gamma^\alpha$ is the accumulated plastic shear on the $\alpha^{\text{th}}$ slip system, the material-dependent parameter $\gamma_{crit}$ controls the damage nucleation, and $m$ is the damage rate sensitivity exponent. The total accumulated slip divided by the factor $(\phi_{nl})^m$ gives the undamaged (effective) plastic strain. Increasing the value of $m$ reduces the stability of the evolution of damage. Details about the phase field model and its coupling with crystal plasticity are described elsewhere (Shanthraj et al., 2016, 2017).

Table 3 gives the material parameters used in the CP simulation. The material properties used to describe the hardening behavior by slip were estimated from the macroscopic stress–strain curves. The ratio between the macroscopic yield stress and the critical resolved shear stress is given by the Taylor factor (Kocks et al., 2000). Therefore, the slip system hardening behavior can be estimated by rescaling the macroscopic stress–strain curve using the Taylor factor. The material properties of the bainite phase were estimated from the macroscopic stress–strain curves of fully bainitic steel. The average Taylor factor for the body-centered cubic crystal structure was set to 2.75. However, because MA islands have a composite microstructure of martensite and austenite, the exact

**Table 3**
Material parameters used in the CP simulations.

|  | Description | Bainite | MA | Unit |
|---|---|---|---|---|
| $C_{11}$ | Elastic constant | $233.3 \times 10^3$ | $417.4 \times 10^3$ | MPa |
| $C_{12}$ | Elastic constant | $135.5 \times 10^3$ | $242.4 \times 10^3$ | MPa |
| $C_{44}$ | Elastic constant | $118.0 \times 10^3$ | $211.1 \times 10^3$ | MPa |
| $\dot{\gamma}_0$ | Reference shear strain rate | $1.0 \times 10^{-3}$ | $1.0 \times 10^{-3}$ | ms$^{-1}$ |
| $S_{0[111]}$ | Slip resistance in [111] slip system | 187 | 526 | MPa |
| $S_{\infty[111]}$ | Saturation slip resistance | 233 | 655 | MPa |
| $S_{0[112]}$ | Slip resistance in [112] slip system | 187 | 526 | MPa |
| $S_{\infty[112]}$ | Saturation slip resistance | 233 | 655 | MPa |
| $h_0$ | Initial hardening rate | 30000 | 563000 | MPa |
| $h_{\alpha,\beta}$ | Interaction parameter | 1.0 | 1.0 |  |
| n | Strain rate exponent | 20 | 20 |  |
| w | Hardening exponent | 2.97 | 2.00 |  |
| M | Damage mobility | 1.0 | – |  |
| $\gamma_{crit}$ | Critical plastic strain for damage | 0.6 | – |  |
| m | Damage rate sensitivity | 10 | – |  |
| l | length scale | 0.06 |  |  |
| D | diffusion tensor ($D_{11} = D_{22} = D_{33}$) | 1.0 | – |  |

mechanical material properties are unclear. To determine the material properties of MA islands for CP analysis, Zambaldi et al. (2012) conducted an inverse analysis with nanoindentation experiments and the CP finite element method (CPFEM). In the present study, nanoindentation experiments were similarly carried out. Table 4 shows the measurement results for the nano hardness in each phase. To prevent constraints from the surrounding bainite matrix, relatively coarse MA islands were selected for the experiment. However, the hardness of MA islands has large scattering, since some unstable austenite in the MA islands causes transformation-induced plasticity (TRIP). The critical resolved shear stresses (initial and saturation value) of the MA phase were predicted based on the hardness ratio between the bainite matrix and the MA islands. The other constitutive parameters of the MA phase were set with reference to the mechanical properties of martensite described by Tasan et al. (2014a).

The material parameters identified in this manner must be determined for each phase in the EBSD measurement area. As mentioned above, the MA islands have a composite microstructure consisting of martensite and austenite. The austenite phase can be identified easily by EBSD measurements, but it is difficult to identify the martensite phase ($\alpha'$) because the bainite phase ($\alpha$) has a similar crystal structure. The strength and area fraction in the secondary phase have large effects on the precision of the stress–strain behavior in a dual-phase microstructure (Calcagnotto et al., 2012; Schemmann et al., 2015). For this reason, the precise identification of the MA area is extremely important in the validation of CP micromechanical analysis.

Tasan et al. (2014a) reported the strain localization analysis of ferrite–martensite dual-phase steel. In their analysis, the image quality (quality of Kikuchi patterns), which is a metric that can be obtained using EBSD, was used to identify the martensite phase. Fig. 3 shows phase separation of bainite and MA constituents. Fig. 3(a) shows the image quality map of the bainite–MA steel. EBSD measurements are strongly dependent on the surface conditions of the specimen. In Fig. 3(a), the image quality map is relatively clear, even though the specimen surface was coated with colloidal SiO$_2$ particles. Generally, for complex crystal structures, such as martensite and grain boundaries, two or more Kikuchi patterns are observed, but the image quality in this case was reduced by the overlap of the Kikuchi patterns. However, when MA islands are identified using a special threshold value for the image quality, it is difficult to apply the same threshold to repolished specimens or to specimens measured using different equipment.

Therefore, in this study, the confidence index (CI) was used to identify each phase. The CI is a reliability index for crystal orientation identification and varies between 0 and 1. A higher CI indicates a more accurate identification of the crystal orientation in an EBSD measurement. Because the CI is a normalized value, it is assumed that fluctuations in the CI caused by the measurement or surface conditions are smaller than fluctuations in the image quality. Furthermore, the CI value in the same grain can be standardized using grain CI standardization, which is a cleanup function commonly used in OIM analysis.

Fig. 3(b) shows an EBSD-based CI map. The regions in this map with high and low reliability indices correspond to the bainite phase and the martensite phase or a grain boundary, respectively. The CI values at grain boundaries were standardized by setting them to the CI value for the corresponding grain obtained using grain CI standardization, as shown in Fig. 3(c). Therefore, the MA islands could be identified separately after grain CI standardization, as shown in Fig. 3(d). Fig. 3(e) shows a phase map in an MA area that was separated using this method. The blue and red areas indicate the retained $\gamma$ phase and the $\alpha$ phase, respectively. The red area was identified as the martensite phase because the $\alpha$ phase in MA is a low-CI area. MA constituents or martensitic islands are visible in the enlarged figure in Fig. 3(e).

**Table 4**
Nano-hardness in each phase.

| Bainite [GPa] | MA [GPa] | Hardness ratio |
|---|---|---|
| 3.2 ± 0.1 | 9.0 ± 2.2 | 2.8 |

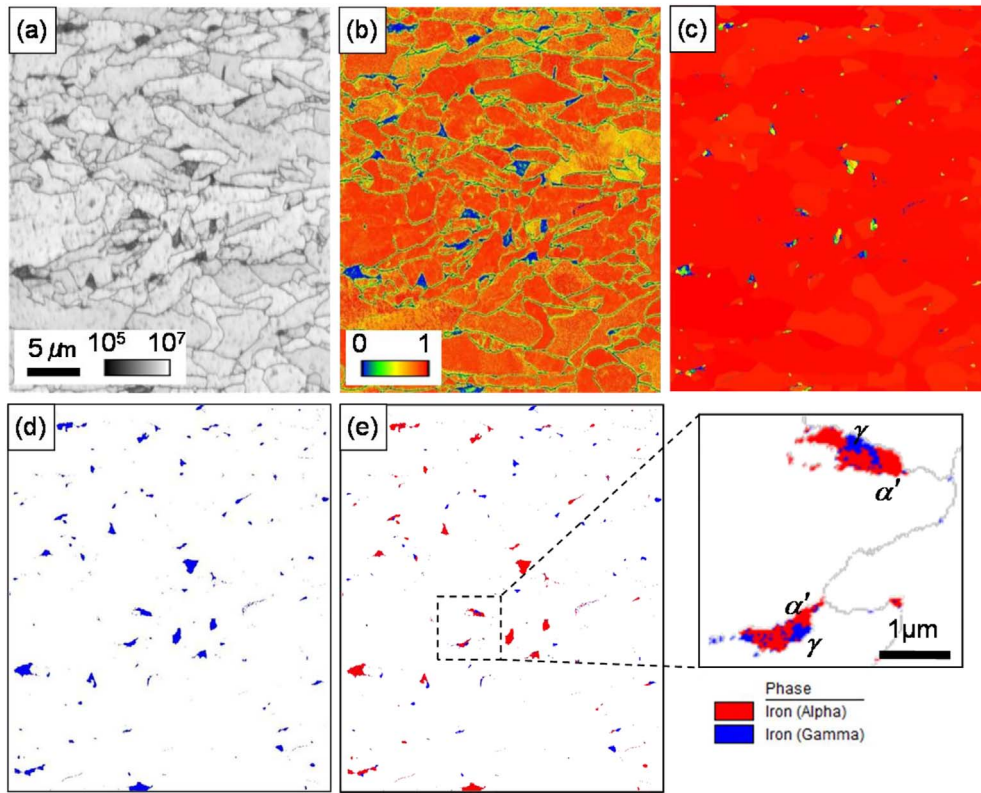**Fig. 3.** Phase separation of bainite and MA constituents.
(a) EBSD-based image quality map.
(b) EBSD-based CI map.
(c) CI map after grain CI standardization.
(d) Threshold of low-order 90% after grain CI standardization.
(e) Phase map of MA constituent area.

Additionally, to reduce the EBSD measurement noise and computation time, all measurement points comprising a grain were replaced by the average orientation for the grain. This replacement, which is a typical cleanup function used in OIM analysis, results in a grain-type aggregate with a single orientation at each constituent measurement point.

In this study, a spectral solver was applied for the CP analysis (Eisenlohr et al., 2013; Shanthraj et al., 2015). From the Green's function method, the equilibrium equations for the first Piola–Kirchhoff stress were solved so as to satisfy both the strain compatibility equations and the boundary conditions. The speed of this calculation is increased by using the fast Fourier transform based solver for the equilibrium equations. This solver can achieve a higher numerical efficiency than the more common finite element method. In addition, the use of the spectral solver in combination with a nonlinear numerical library improves the convergence of the simulation. The boundary conditions are based on the periodic boundary conditions because trigonometric polynomials were used as the basis functions. The periodic boundary conditions express the bulk characteristics by arranging image cells periodically around the calculation field and thus eliminate the influence of the free surface.

However, the surface of the tensile specimens used in the DIC analysis is a free surface. Therefore, in the spectral solver, a low-stiffness layer was placed on top of the calculation layer to mimic the free surface. The low-stiffness layer has a thickness of two Fourier points and is isotropic linear elastic with $c_{11} = 417.4$ Pa and $c_{12} = 242.4$ Pa. The calculation layer for the microstructure was extruded to three Fourier points (i.e., the columnar grain assumption was applied). The crystal orientation used in the spectral solver was rotated so that it matched the EBSD, specimen, and spectral solver coordinate systems in turn. The numerical conditions were set equal to those in the experiment, and a strain rate of $2.5 \times 10^{-4}$ s$^{-1}$ and a simulation time of 400 s were used. The peripheral boundary conditions of the EBSD microstructure were set to be uniaxial tensile strain. Also, the out-of-plane direction of the EBSD microstructure was set to be stress-free to reflect the experimental condition of a free surface.

## 3. Results

### 3.1. Experimental results

Fig. 4 shows SEM micrographs taken at different stages of tensile deformation ($\bar{\varepsilon}_x = 0.00$, 0.06, and 0.11 from left to right).
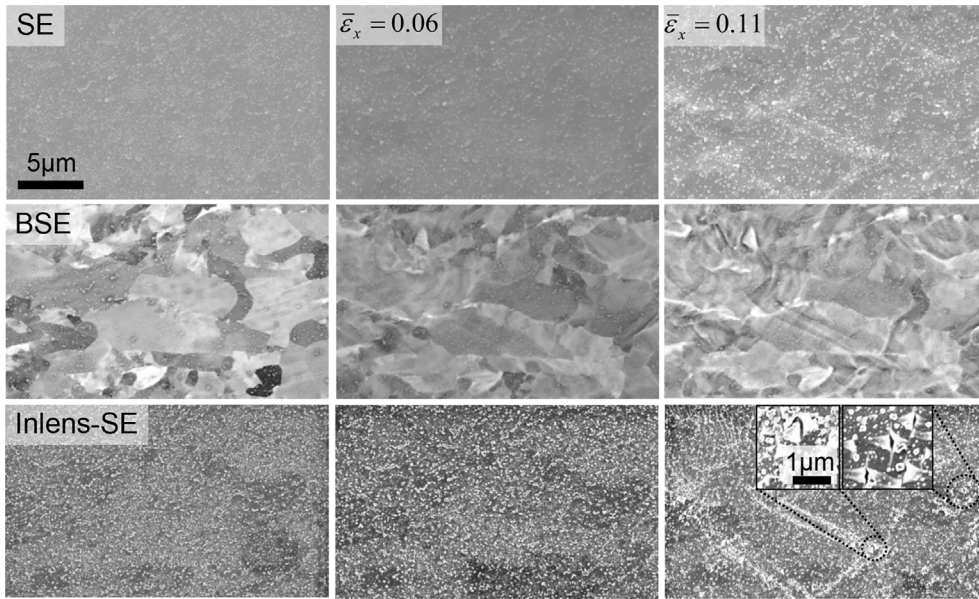
**Fig. 4.** SEM micrographs at different tensile deformation stages.

Different images were recorded by the SE, BSE, and in-lens SE detectors, as shown here. In the SE images at a tensile strain of $\bar{\varepsilon}_x = 0.11$, surface roughening was observed, especially in bands oriented at 45° with respect to the tensile direction. This is a first indicator of the heterogeneous nature of plastic deformation. BSE images of the same field were used to match the strain and EBSD maps. The in-lens SE images were used for the DIC analysis and to map nano- or microcracks on the specimen surface.

Fig. 5 shows the inverse pole figure maps at different tensile deformation stages from the EBSD results mentioned above and from the CP simulation results, which are presented below. When the tensile strain reached $\bar{\varepsilon}_x = 0.11$, non-indexed points were observed in EBSD map because of the large plastic deformation.

Fig. 6 shows the strain mapping results from the experiments and simulations at different tensile deformation stages. Fig. 6(a) shows the high-angle (i.e., more than 15°) grain boundary superimposed on strain maps from DIC, and Fig. 6(b) shows the CP strain results calculated using the spectral solver. The strain contour is displayed in units of equivalent von Mises strain. MA islands, which are colored black, were identified using the method described in the previous section. The DIC field contains more than 10 MA islands of different sizes.

The μ-DIC method provides a spatial strain mapping resolution of 100 nm. It is expected that various strain bands exist where the deformation is localized. The areas that experienced the highest local strain are the highly strained shear band region and the microcrack area displayed in the in-lens SE images. The von Mises strain in the uncolored areas exceeds the maximum von Mises
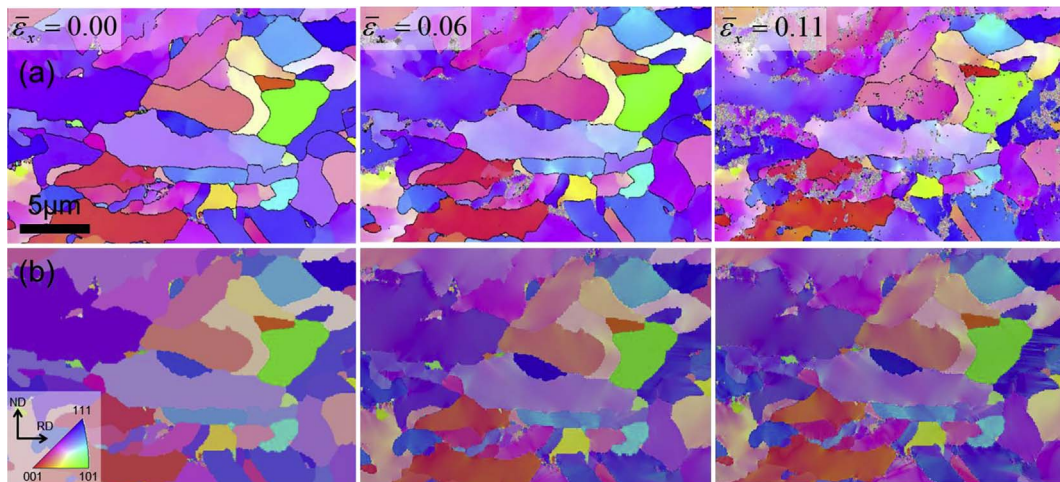


**Fig. 5.** Inverse pole figure maps at different tensile deformation stages.
(a) EBSD measurement results.
(b) Simulation results for the texture evolution obtained using the spectral solver.
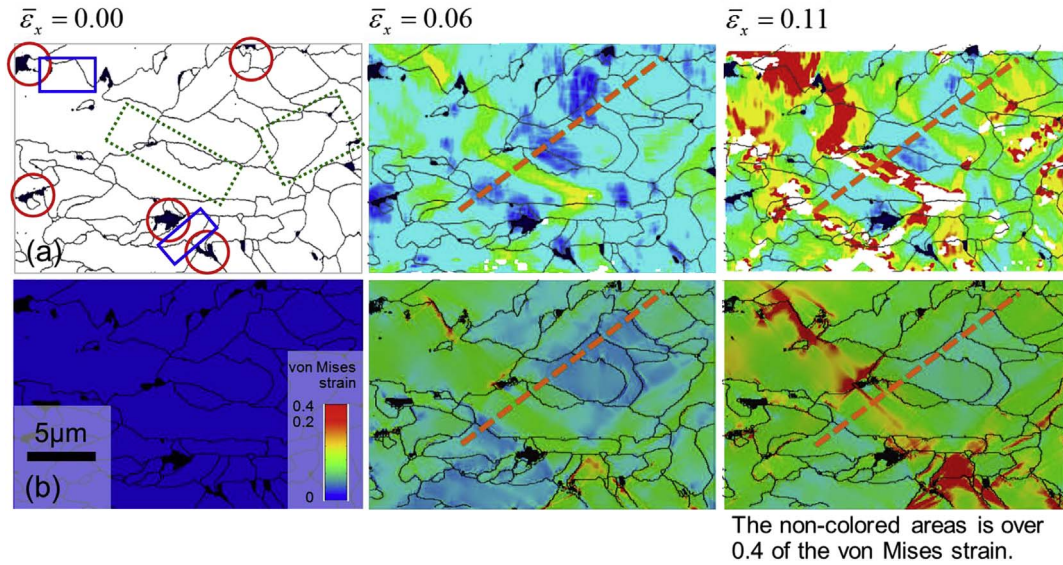
**Fig. 6.** Strain maps at different tensile deformation stages.
MA constituent regions shown in black.
(a) μ-DIC strain map with grain boundaries.
(b) Simulation results obtained using the spectral solver.

strain ($\varepsilon_{Mises} = 0.4$) that could be measured in the DIC experiments. As plastic deformation proceeds, the areas around the strain localization zones are emphasized without homogeneous deformation, and heterogeneous deformation occurs (Jia et al., 2012a, 2012b, 2014). Also, the non-indexed areas in Fig. 5 mainly correspond to the strain localization areas at a global strain of $\bar{\varepsilon}_x = 0.11$.

Next, the strain localization zones in the vicinity of the MA islands were evaluated. The strain levels around the MA islands were lower than those in the matrix bainite phase (e.g., the red circles in Fig. 6(a)). However, in areas between coarser MA islands, severe strain localization was observed (e.g., blue rectangles in Fig. 6(a)). Zones with highly localized deformation were also observed in bainite regions that do not surround MA islands (e.g., green rectangles in Fig. 6(a)).

Fig. 7 shows the von Mises strain distributions in each phase obtained from the experimental and simulation results. The simulation results are discussed in the next section. The fraction of microstructural areas with a specific von Mises strain is given in Fig. 7(a) and (b) for the bainite phase and the MA islands, respectively. In both phases, the area fraction increases greatly and reaches a peak, then decreases gradually as the von Mises strain increases. The distribution functions follow a near-logarithmic shape. The bainite phase carries the majority of the plastic strain, and the MA islands are only weakly deformed. In the bainite phase, the distribution of the von Mises strain broadens as the plastic strain increases, promoting heterogeneous deformation. Table 5 gives the von Mises strain distributions in the histograms in Fig. 7. The maximum von Mises strain in the bainite phase reached over 0.7 at a tensile strain of $\bar{\varepsilon}_x = 0.11$.

Fig. 8 shows quantitative line profiles (e.g., the orange broken lines in Fig. 6) of the von Mises strain at different deformation stages obtained from the experimental and simulation results. The simulation results are discussed in the next section. The
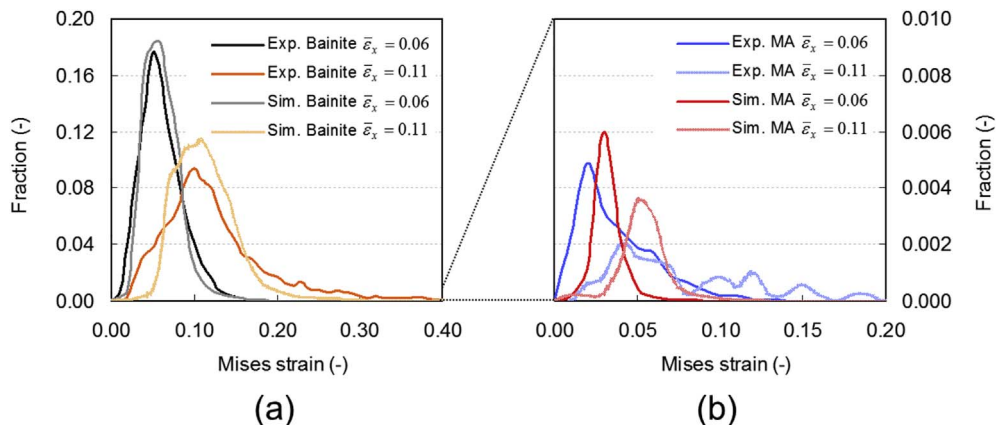


**Fig. 7.** Von Mises strain histograms obtained from the μ-DIC and CP simulation results in each phase. (a) Bainite phase, (b) MA constituent islands.

**Table 5**

Von Mises strain distributions in the histograms in Fig. 7.

| Phase | Global strain | Average | Maximum | Minimum |
|---|---|---|---|---|
| **Experiment** | | | | |
| Bainite | 0.06 | 0.056 | 0.158 | 0.001 |
| Bainite | 0.11 | 0.123 | 0.719 | 0.004 |
| MA | 0.06 | 0.033 | 0.130 | 0.003 |
| MA | 0.11 | 0.067 | 0.148 | 0.013 |
| **Simulation** | | | | |
| Bainite | 0.06 | 0.066 | 0.415 | 0.0003 |
| Bainite | 0.11 | 0.120 | 0.761 | 0.0003 |
| MA | 0.06 | 0.026 | 0.183 | 0.0002 |
| MA | 0.11 | 0.038 | 0.219 | 0.0002 |
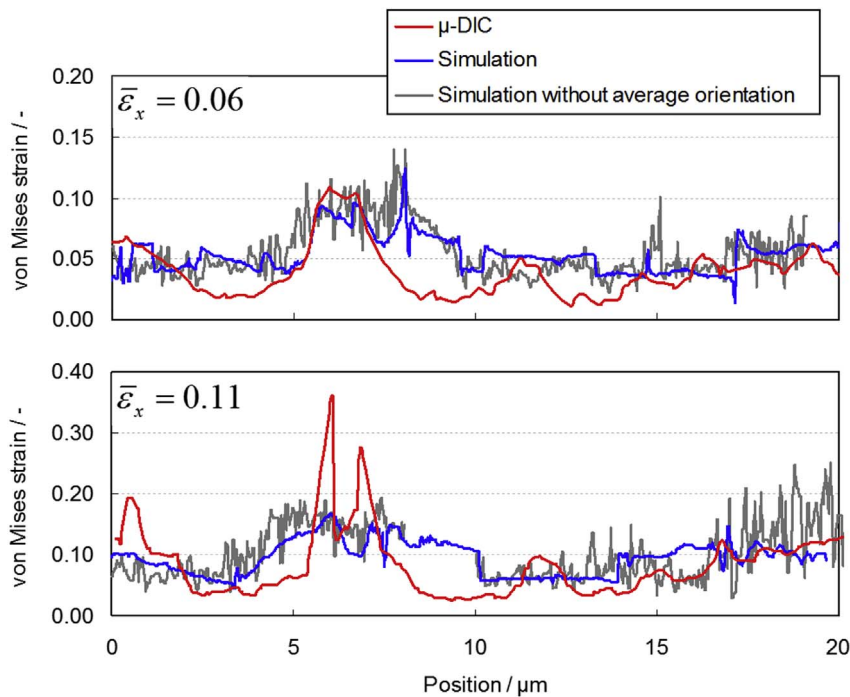


**Fig. 8.** Line profiles of the von Mises strain at different deformation stages.

experimental results indicate that the bainite phase shows strain heterogeneity and locally sharp strain gradients. Additionally, the strain gradients increased with increasing plastic deformation.

### 3.2. Simulation results

Fig. 6(b) shows the strain mapping results obtained from the spectral CP simulations. The high-equivalent-strain regions obtained from the simulation results show rough correspondence with those obtained from the results of the DIC experiments (Fig. 6(a)), indicating reasonable agreement and adequate constitutive formulations. However, the accuracy in the low-equivalent-strain regions is insufficient.

Fig. 7 shows the von Mises strain histograms obtained by the spectral CP simulation for each phase. The average peaks of the von Mises strain histogram obtained from the simulation are almost identical to those from μ-DIC for the bainite phase, as shown in Table 5. Therefore, the constitutive parameters used for the CP simulations reflect the average bainite mechanical response in a reasonable fashion. On the other hand, the average peaks of the von Mises strain in the MA islands were slightly larger than those obtained experimentally. The constitutive parameters in the MA islands were estimated from the nanoindentation experiment and the martensite properties in ferrite–martensite dual-phase steel. Moreover, the histograms obtained from the simulation for the MA islands showed a narrower range than those from the experimental results. This indicates that actual MA islands have a large plastic
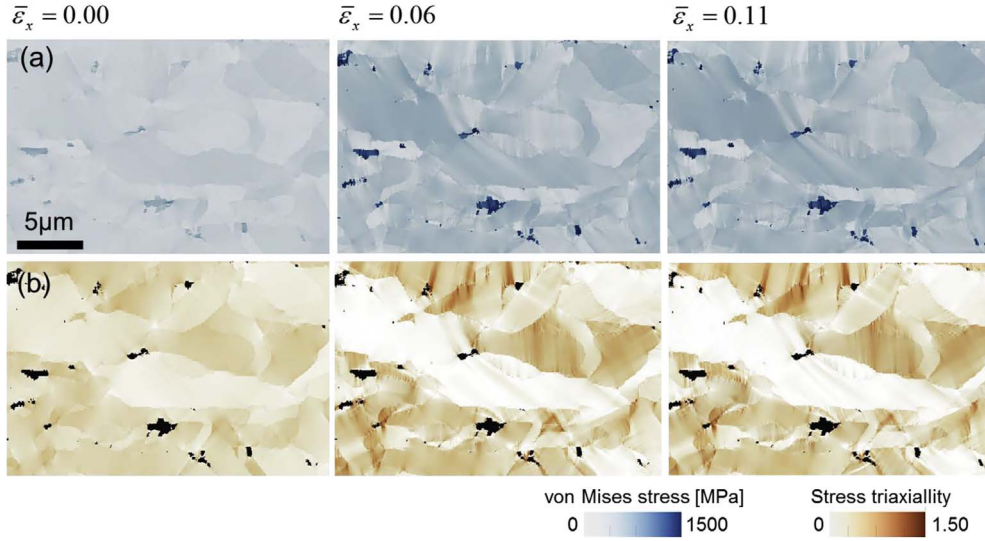
**Fig. 9.** Stress map obtained from spectral CP simulations at different tensile deformation stages.
(a) Von Mises stress, (b) Stress triaxiality.

deformation distribution and are harder than the estimated martensite phase.

Fig. 8 shows the line profiles of the von Mises strain obtained from the spectral CP simulation for the bainite phase. The simulation results without the average orientation are discussed in the discussion section of this paper. The average von Mises strain of the bainite phase obtained from the simulation is in good agreement with that from the experiment, as shown in Fig. 7 and Table 5. However, the simulated profile of the von Mises strain is flatter and has a more narrow strain distribution than the experimental profile.

The simulation has the advantage of enabling the evaluation of the distributions of both the stress and the strain. Fig. 9(a) and (b) show the predicted equivalent stress and the stress triaxiality, respectively, obtained from the simulation. The simulation results are shown at different deformation stages ($\bar{\varepsilon}_x = 0.01$, 0.06, and 0.11 from left to right). Fig. 9(a) shows that the equivalent stress is high at the MA islands. The MA islands carry higher tensile stresses because of the stress partitioning between bainite and MA grains. The stress triaxiality (Fig. 9(b)) is defined as the ratio of the average stress to the equivalent stress, as

$$\frac{\sigma_H}{\sigma_{EQ}} = \frac{(\sigma_1 + \sigma_2 + \sigma_2)/3}{\sqrt{\frac{1}{2}\{(\sigma_1 - \sigma_2)^2(\sigma_2 - \sigma_3)^2 + (\sigma_3 - \sigma_1)^2\}}} \tag{9}$$

where $\sigma_H$ is the hydrostatic stress; $\sigma_{EQ}$ is the equivalent stress; and $\sigma_1$, $\sigma_2$, and $\sigma_3$ are the normal stresses in the x-, y-, and z-directions, respectively. The void nucleation behavior in ductile fracture influences the stress triaxiality (Hancock and Makenzie, 1976). Therefore, ductile fracture occurs more readily when the stress triaxiality is high.

Fig. 10(a) and (b) shows the ductile crack initiation map after strain localization obtained from the experimental and CP simulation results, respectively, at a global strain of $\bar{\varepsilon}_x = 0.11$. Also, Fig. 11(a) and (b) show the ductile crack initiation map after strain
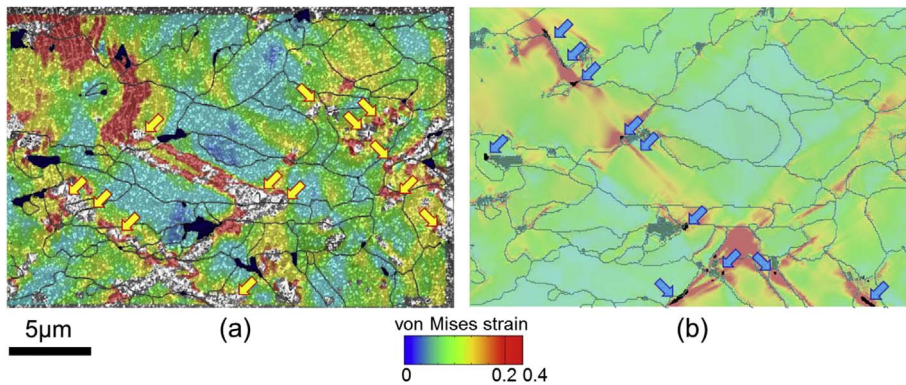


**Fig. 10.** Comparison of damage nucleation sites obtained from the experimental and CP simulation results at a global strain of $\bar{\varepsilon}_x = 0.11$.
(a) Experimental von Mises strain map superimposed on the in-lens SE image.
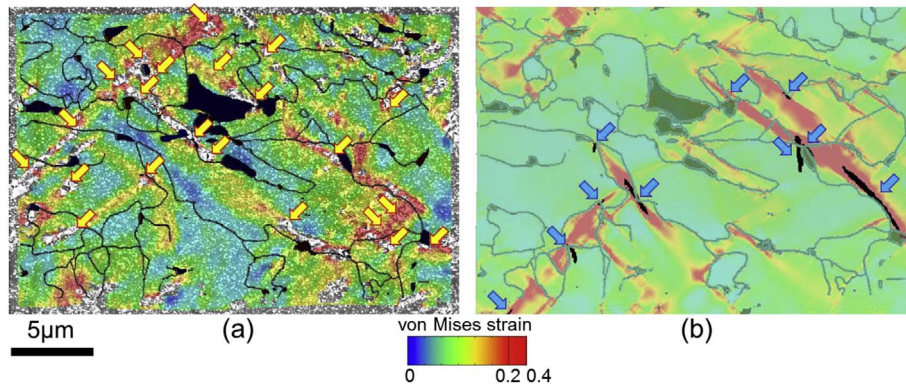(b) Numerical von Mises strain map.

**Fig. 11.** Damage nucleation sites obtained from the experimental and CP simulation results of the bainite matrix with coarse MA at a global strain of $\bar{\varepsilon}_x = 0.11$.
(a) Experimental von Mises strain map superimposed on the in-lens SE image.
(b) Numerical von Mises strain map.

localization obtained from the experimental and CP simulation results of the bainite matrix with coarse MA, respectively, at a global strain of $\bar{\varepsilon}_x = 0.11$. In the experimental results, the ductile crack sites were identified from an in-lens SE image (e.g., yellow arrows in Figs. 10(a) and 11(a)). In the simulation results, the ductile crack sites were obtained using the ductile damage criterion (e.g., blue arrows in Figs. 10(b) and 11(b)), as shown in Eq. (8). In the case shown in Figs. 10 and 11, the ductile crack sites identified using both methods correspond to the strain localization area; however, this is not always the case.

## 4. Discussion

The heterogeneity of the plastic deformation in bainite–MA steel used for linepipe applications was quantitatively evaluated using a joint numerical–experimental approach based on a combination of μ-DIC experiments and CP simulations using a spectral solver. The μ-DIC method, in which the displacement of colloidal $SiO_2$ particles with plastic deformation is determined using in-lens SE images, achieved a high strain resolution of 100 nm. This approach demonstrated that the strain localization around fine secondary-phase particles in dual-phase steel can be evaluated quantitatively (Tasan et al., 2014a, 2014b; Yan et al., 2015). In particular, μ-DIC yields a quantitative description of the internal deformation behavior of MA regions, which is challenging to track using conventional approaches. The strain maps obtained using the μ-DIC method adequately reflect the local micromechanical deformation behavior in this material. However, slight deviations between the current model experiments and the actual material response may result from the fact that the μ-DIC strain patterns were derived using a plane stress approximation. To accurately determine the plastic strain distribution and dynamic characteristics, a tomographic determination of the strain distribution may be necessary. Moreover, the μ-DIC technique reveals that it is difficult to capture the high plastic strain (The non-colored areas in Fig. 6; e.g., $\bar{\varepsilon}_x = 0.11$). Wang et al. (2015) proposed that the HRTEM-DIC analysis provides nanoscale characterization capabilities that are not possible with SEM-based DIC. On the other hands, it is not easy to specify the strain localization areas before deformation. It is assumed that the DIC measurements at the different scales are effective for capturing both the mesoscale strain localization and the nucleation of micro crack as Wang et al. (2015) also proposed.

During the early deformation stage (Fig. 6; e.g., $\bar{\varepsilon}_x = 0.06$), strain localization occurred around the bainite grains and close to the bainite grain boundaries, but there was no strain localization around the MA islands. Furthermore, small microcracks on the surface of the specimen were observed in the in-lens SE image shown in Fig. 4. Comparing regions of crack events with those of pronounced strain localization revealed that the cracks formed in the bainite phase, which has a high von Mises strain. Strain maps have been reported for ferrite–martensite (Tasan et al., 2014a, 2014b; Yan et al., 2015) and ferrite–bainite (Ishikawa et al., 2015) dual-phase steel. Both of these dual-phase steels have a relatively large secondary phase volume fraction and show strain localization around regions where coarse islands of the secondary phase are in close proximity. However, the secondary phase of the bainite–MA steel considered in this study has a low volume fraction and small morphological features, as shown in Table 2. Furthermore, as explained later, the MA islands have the same hardenability as the bainite phase in the early deformation stages. Therefore, the deformation restriction causes by the presence of MA islands is relatively weak. It is presumed that this situation caused strain localization around the bainite grains and close to the bainite grain boundaries.

Additionally, the grain boundary characteristics and three-dimensional grain structure are plausible causes for the initiation of strain localization in the bainite phase. Moreover, it is assumed that bainite grains that are near MA islands can be softened partially because of the carbon enrichment of the untransformed austenite from the bainite phase enabled by the heat treatment after accelerated cooling.

As the regions in which relatively coarse MA islands are in close proximity experience a high deformation gradient as the plastic deformation increases, the grain size and distribution of the MA islands both influenced the strain localization and are found to be important factors in the optimization of the mechanical response of these steels. Tsuyama et al. (2013) have reported differences between the toughnesses of the MA islands and the matrix. The finely dispersed MA islands produced by the online heat process are

based on the retained austenite and are adjacent to grains that have variable K–S variants after the formation of MA islands. Such discontinuous boundary characteristics show the prevention of crack propagation around MA islands. Therefore, it was assumed that the characteristics of the grain boundary between the bainite matrix and the MA islands can influence the propagation, localization, and patterning of plastic deformation.

The histograms in Fig. 7 reveal that the bainite matrix carries the majority (98%) of the plastic strain. Low-strain regions exist in the MA islands, and the von Mises strain distribution in the MA islands extended over the high-strain area when the tensile strain reached $\bar{\varepsilon}_x = 0.11$. High-strain regions exist locally in the MA islands, and it can be assumed that the most of the high-strain regions consist of the retained austenite phase. Furthermore, the difference between the average von Mises strains of the two phases is only 0.02, as shown in Table 5 (e.g., experimental results of $\bar{\varepsilon}_x = 0.06$), and the difference between the maximum von Mises strains of the two phases was also very small. Therefore, the MA islands showed micromechanical deformation behavior similar to that of the bainite grains during the early deformation stage with the deformation of retained austenite and gradually assumed the role of the hardening phase as the plastic deformation increases.

On the other hand, the increase in the von Mises strain in the MA islands as a function of the global strain is smaller than that in the bainite phase. This suggests that the work hardening rate in the MA islands increases more rapidly with ongoing plastic deformation. In this situation, the bainite matrix experiences compressive stresses after the MA islands yield because its work hardening rate is less than that of the MA islands. Conversely, the MA islands carry more tensile stress as a result of the tensile stress distribution among the bainite phase and the MA islands. This observation suggests that the large work hardenability of this material is produced by the combination of both this stress distribution and work hardening with a local strain gradient in each phase.

The strain mapping results obtained from μ-DIC and from the spectral solver are shown in Fig. 6. Rough correspondence between the experimental and numerical results was observed for the high-equivalent-strain regions (warm-colored areas in Fig. 6) and the starting point of strain localization (yellow area at $\bar{\varepsilon}_x = 0.06$ in Fig. 6). These effects are adequately captured by the CP predictions. The underlying constitutive parameters are appropriate because the distribution peaks of the von Mises strain obtained from μ-DIC and the spectral solver roughly agree. Moreover, as shown in Fig. 5(b), the simulation results of the crystal orientation evolution provide important information because grain rotations are hard to map by EBSD when the material has undergone large local distortions.

Tasan et al. (2014a) reported the strain localization analysis of ferrite–martensite dual-phase steel and discussed the differences between the experimental strain mapping results and those obtained from a CP simulation. These differences were mainly caused by differences in the three-dimensional microstructures considered in the experiment and simulation (e.g., the secondary phase in the experiment is thin and flat compared to the simulation). In the present study, the three-dimensional microstructure was idealized in the spectral solver as a columnar microstructure because the calculation layer for the microstructure was extruded to three Fourier points with identical material properties. This approach assumes that the actual in-plane microstructure evaluated by μ-DIC had an approximately columnar microstructure at least over a certain layer thickness beneath the mapped sample surface. Furthermore, the strain localization starting points in the simulation and experimental results roughly agreed in spite of the fact that the CP simulation does not consider specific constitutive laws for the grain boundary properties, except the kinematical ones captured implicitly by the change in orientation. This means that strain localization in the current case depends on the grain morphology and crystal orientation.

The ductile crack initiation maps after strain localization were obtained experimentally and numerically (e.g. Figs. 10 and 11). The two maps coincide in terms of the presence of ductile crack initiation sites around the strain localization region, but the ductile crack initiation sites do not always correspond. Some experimental works (Aswath, 1994; Marchal et al., 2006) suggest that crack formation is strongly dependent on strain localization in specific crystallographic planes. Antolovich et al. (1993) reveal that while damage accumulation in slip planes may contribute to initiation of damage, its propagation can take place in other (non-slip) crystallographic planes as well. Extension of the anisotropic ductile model, to explain the disagreement between the experiment and simulation may be considered in future. Moreover, the prediction of damage initiation sites also relies on accurate prediction of stress and strain fields. As mentioned above, the morphology of the three-dimensional microstructure can produce an apparent fluctuation in the critical shear slip under ductile damage. Additionally, it is assumed that the matrix hardness fluctuations caused by carbon diffusion during heat processing also affect the ductile crack initiation.

The influence of MA island sizes on strain localization of bainite matrix were compared between Figs. 10 and 11. Both microstructures show strain bands oriented at 45° with respect to the tensile direction. Especially, the strain bands are concentrated surrounding the regions in which relatively coarse MA islands (approximately 5 μm) are in close proximity, as shown in Fig. 11(a). Such a local difference of plastic behavior is compensated by the large work hardenability of this material. Therefore, finely dispersed MA islands are useful for the prevention of excessive or heterogeneous strain localization and can contribute to the improvement of the strain capacity of bainite–MA steel.

There are points where the accuracy of the spectral solver can be improved. For example, the accuracy in the low-equivalent-strain region (cold-colored area in Fig. 6) is insufficient. As shown in Fig. 8, the simulated line profiles of the bainite phase indicated a flatter von Mises strain distribution than the experimental results. Zhang et al. (2016) also reported that the experiments have the stronger localizations of strain than the simulations in superalloys. This means that the current simulation results predict a more homogeneous deformation than that in the actual experimental results. Both the experimental and simulation results suggest that the crystal orientation influences strain localization effects (Raabe et al., 2001). As mentioned before, an average (single) orientation processing was applied to identify individual grains in the CP analysis. Therefore, the slight misorientations that are typically present in each grain have not been considered. The influence of the average orientation used in the CP simulation was evaluated using the original crystal orientation before averaging. Fig. 12 shows the numerical strain mapping results without applying the average
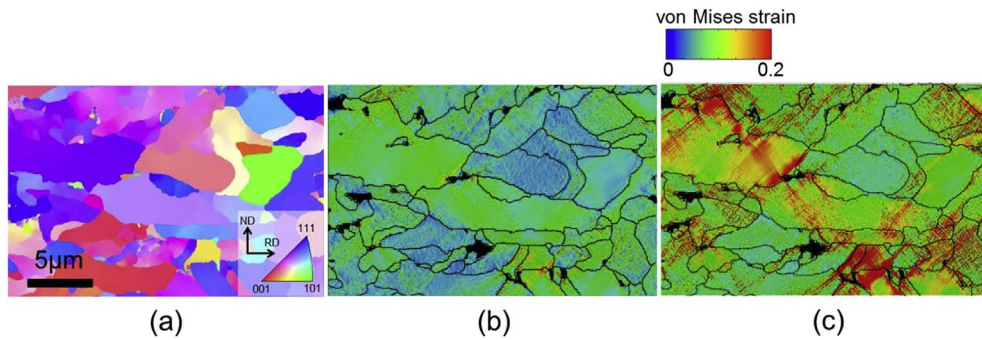
**Fig. 12.** Numerical strain mapping results without applying the average crystal orientation per grain.
(a) Inverse pole figure map, von Mises strain map at a global strain of
(b) $\bar{\varepsilon}_x = 0.06$, (c) $\bar{\varepsilon}_x = 0.11$.

orientation per grain. The location of the strain localization around the bainite grain boundary does not significantly differ from that of the strain mapping results of the simulation with average orientation processing (Fig. 6(b)). Additionally, the line profiles of the von Mises strain showed only small fluctuations, as shown in Fig. 8. This means that the observed strain localization depends not on slight misorientations but on the average orientation per grain.

Because the MA islands have a composite microstructure consisting of martensite and austenite, as shown in Fig. 3(e), the identification of their mechanical properties are also important. In this study, the mechanical properties of the MA islands were expressed by the nanoindentation experiment and the material parameters obtained in previous studies (Tasan et al., 2014a). The mechanical properties of martensite are sensitive to the chemical composition of the steel (e.g., especially carbon content) and the heat treatment history. A multiphysics approach including chemical composition (e.g., carbon distribution map by a high-resolution EPMA) may be considered in future. Finally, the TRIP effect should be taken into account in future constitutive formulations. Although some atomic-scale data are necessary (e.g., stacking fault energy and the Gibbs free energy), a recently introduced TRIP constitutive model may be well suited for this purpose (Ma and Hartmaier, 2015; Wong et al., 2016).

## 5. Conclusions

The heterogeneous plastic micromechanical deformation in bainite–MA steel commonly used for linepipe was quantitatively evaluated. A joint numerical–experimental approach was employed by combining μ-DIC experiments with a CP-based spectral simulation. The μ-DIC method, in which the displacement of colloidal $SiO_2$ particles with proceeding plastic deformation is tracked using in-lens SE images, achieved a high strain resolution of 100 nm, enabling the discrimination of strain localization phenomena around fine secondary-phase particles.

The strain mapping results obtained from μ-DIC and the spectral solver were then compared. Rough correspondence was observed between the high-equivalent-strain regions and the starting point of strain localization, validating the effectiveness of this joint approach. The ductile crack initiation maps coincide in terms of the presence of ductile crack initiation sites around the strain localization region, but the ductile crack initiation sites do not always correspond. This indicates that the ductile damage initiation of bainite matrix has considerable anisotropy.

During the early deformation stage, strain localization occurred around the bainite grains and close to the bainite grain boundaries. Moreover, MA islands showed micromechanical deformation behaviors similar to those of the bainite grains during the early deformation stage and gradually assumed the role of the hardening phase as the plastic deformation increased. Such that the difference of plastic behavior is a unique compared with that of harder secondary phase in other dual phase steels, and is compensated by the large work hardenability of this material. However, coarse MA islands (approximately > 5 μm) trigger strain localization. In contrast finely dispersed MA islands prevent excessive or heterogeneous strain localization and can contribute to the improvement of the strain capacity of bainite–MA steel for a new strain-based linepipe design approach.

## References

Antolovich, B.F., Saxena, A., Antolovich, S.D., 1993. Fatigue crack propagation in single-crystal CMSX-2 at elevated temperature. J. Mater. Eng. Perform. 2 (4), 489–495.

Aswath, P.B., 1994. Effect of orientation on crystallographic cracking in notched nickelbase superalloy single crystal subjected to far-field cyclic compression. Metall. Mat. Trans. A 25 (2), 287–297.

Bertin, M., Du, C., Hoefnagels, J.P.M., Hild, F., 2016. Crystal plasticity parameter identification with 3D measurements and integrated digital image correlation. Acta Mater. 116, 321–331.

Calcagnotto, M., Ponge, D., Demir, E., Raabe, D., 2010. Orientation gradients and geometrically necessary dislocations in ultrafine grained dual-phase steels studied by 2D and 3D EBSD. Mater. Sci. Eng. A527, 2738–2746.

Calcagnotto, M., Adachi, Y., Ponge, D., Raabe, D., 2011. Deformation and fracture mechanisms in fine- and ultrafine-grained ferrite/martensite dual-phase steels and the effect of aging. Acta Mater. 59, 658–670.

Calcagnotto, M., Ponge, D., Raabe, D., 2012. Microstructure control during fabrication of ultrafine grained dual-phase steel: characterization and effect of intercritical annealing parameters. ISIJ Int. 52, 874–883.

Eisenlohr, P., Diehl, M., Lebensohn, R.A., Roters, F., 2013. A spectral method solution to crystal elasto-viscoplasticity at finite strains. Int. J. Plast. 46, 37–53.

Fan, L., Zhou, D., Wang, T., Li, S., Wang, Q., 2014. Tensile properties of an acicular ferrite and martensite-austenite constituent steel with varying cooling rates. Mater. Sci. Eng. A590, 224–231.

Gioacchino, F.D., Clegg, W.J., 2014. Mapping deformation in small-scale testing. Acta Mater. 78, 103–113.

Guan, Y., Chen, B., Zou, J., Britton, T.B., Jiang, J., Dunne, F.P.E., 2017. Crystal plasticity modelling and HR-DIC measurement of slip activation and strain localization in single and oligo-crystal Ni alloys under fatigue. Int. J. Plast. 88, 70–88.

Guery, A., Hild, F., Latourte, F., Roux, S., 2016. Slip activities in polycrystals determined by coupling DIC measurements with crystal plasticity calculations. Int. J. Plast. 81, 249–266.

Han, Q., Kang, Y., Hodgson, P.D., Stanford, N., 2013. Quantitative measurement of strain partitioning and slip systems in a dual-phase steel. Scripta Mater. 69, 13–16.

Hancock, J.,W., Makenzie, A.,C., 1976. On the mechanisms of ductile failure in high-strength steels subject to multi-axial stress-states. J. Mech. Phys. Solid. 24, 141–169.

Ishikawa, N., Sueyoshi, H., Endo, S., Shikanai, N., 2005. Effect of microstructure on deformation behavior of ferrite-bainite steels. Tetsu-To-Hagane 91, 809–815.

Ishikawa, N., Shinmiya, T., Igi, S., Kondo, J., 2006. Toughness evaluation on seam weld HAZ of high strength UOE linepipe. In: Proc. 6th International Pipeline Conference, pp. 223–230.

Ishikawa, N., Shimamura, J., Yasuda, K., Nakamichi, H., Endo, S., Tsuyama, S., 2014. Microstructural aspects of Bainite-MA type dual-phase steel for the strain-based design in terms of deformation and fracture. In: Proc. 24th International Ocean and Polar Engineering Conference, pp. 205–512.

Ishikawa, N., Yasuda, K., Sueyoshi, H., Endo, S., Ikeda, H., Morikawa, T., Higashida, K., 2015. Microscopic deformation and strain hardening analysis of ferrite–bainite dual-phase steels using micro-grid method. Acta Mater. 97, 257–268.

Jia, N., Roters, F., Eisenlohr, P., Kords, C., Raabe, D., 2012a. Non-crystallographic shear banding in crystal plasticity FEM simulations: example of texture evolution in α-brass. Acta Mater. 60, 1099–1115.

Jia, N., Eisenlohr, P., Roters, F., Raabe, D., Zhao, X., 2012b. Orientation dependence of shear banding in face-centered-cubic single crystals. Acta Mater. 60, 3415–3434.

Jia, N., Raabe, D., Zhao, X., 2014. Texture and microstructure evolution during non-crystallographic shear banding in a plane strain compressed Cu-Ag metal matrix composite. Acta Mater. 76, 238–251.

Kadkhodapour, J., Schmauder, S., Raabe, D., Ziaei-Rad, S., Weber, U., Calcagnotto, M., 2011. Experimental and numerical study on geometrically necessary dislocations and non-homogeneous mechanical properties of the ferrite phase in dual phase steels. Acta Mater. 59, 4387–4394.

Kocks, U.F., Tomé, C.N., Wenk, H.-R., 2000. Texture and Anisotropy. Cambridge University Press.

Lan, L., Qiu, C., Song, H., Zhao, D., 2014. Correlation of martensite–austenite constituent and cleavage crack initiation in welding heat affected zone of low carbon bainitic steel. Mater. Lett. 125, 86–88.

Li, X., Shang, C., Ma, X., Gault, B., Subramanian, S.V., Sun, J., Misra, R.D.K., 2017. Elemental distribution in the martensite–austenite constituent in intercritically reheated coarse-grained heat-affected zone of a high-strength pipeline steel. Scripta Mater. 139, 67–70.

Ma, A., Hartmaier, A., 2015. A study of deformation and phase transformation coupling for TRIP-assisted steels. Int. J. Plast. 64, 40–55.

Marchal, N., Flouriot, S., Forest, S., Remy, L., 2006. Crack-tip stress–strain fields in single crystal nickel-base superalloys at high temperature under cyclic loading. Comput. Mat. Sci. 37, 42–50.

Minami, H., Ikeda, H., Morikawa, T., Higashida, K., Mayama, T., Toji, Y., Hasegawa, K., 2012. Visualization of plastic strain distribution in a dual-phase steel using high-precision grid-markers. Tetsu-To-Hagane 98, 303–310.

Morooka, S., Umezawa, O., Harjo, S., Hasegawa, K., Toji, Y., 2012. Quantitative analysis of tensile deformation behavior by in-situ neutron diffraction for ferrite-martensite type dual-phase steels. Tetsu-To-Hagane 98, 311–319. https://doi.org/10.2355/tetsutohagane.98.311.

Peirce, D., Asaro, R.J., Needleman, A., 1982. An analysis of nonuniform and localized deformation in ductile single crystals. Acta Metal 30, 1087–1119.

Raabe, D., 1995a. Simulation of rolling textures of b.c.c. metals considering grain interactions and crystallographic slip on {110}, {112} and {123} planes. Mater. Sci. Eng. A197, 31–37.

Raabe, D., 1995b. Investigation of contribution of {123} slip planes to development of rolling textures in bee metals by use of Taylor models. Mater. Sci. Technol. 11, 455–460.

Raabe, D., Sachtleber, M., Zhao, Z., Roters, F., Zaefferer, S., 2001. Micromechanical and macromechanical effects in grain scale polycrystal plasticity experimentation and simulation. Acta Mater. 49, 3433–3441.

Raabe, D., Sachtleber, M., Weiland, H., Scheele, G., Zhao, Z., 2003. Grain-scale micromechanics of polycrystal surfaces during plastic straining. Acta Mater. 51, 1539–1560.

Reuber, C., Eisenlohr, P., Roters, F., Raabe, D., 2014. Dislocation density distribution around an indent in single-crystalline nickel: comparing nonlocal crystal plasticity finite-element predictions with experiments. Acta Mater. 71, 333–348.

Roters, F., Raabe, D., Gottstein, G., 2000. Work hardening in heterogeneous alloys - a microstructural approach based on three internal state variables. Acta Mater. 48, 4181–4189.

Roters, F., Eisenlohr, P., Hantcherli, L., Tjahjanto, D., Bieler, T., Raabe, D., 2010. Overview of constitutive laws, kinematics, homogenization and multiscale methods in crystal plasticity finite-element modeling: theory, experiments, applications. Acta Mater. 58, 1152–1211.

Roters, F., Eisenlohr, P., Kords, C., Tjahjanto, D., Diehl, M., Raabe, D., 2012. DAMASK: the Düsseldorf advanced material simulation kit for studying crystal plasticity using an FE based or a spectral numerical solver. In: In: Cazacu, O. (Ed.), Procedia IUTAM: IUTAM Symposium on Linking Scales in Computation: from Microstructure to Macroscale Properties, vol. 3. Elsevier, Amsterdam, pp. 3–10.

Sachtleber, M., Zhao, Z., Raabe, D., 2002. Experimental investigation of plastic grain interaction. Mater. Sci. Eng. A336, 81–87.

Schemmann, L., Zaefferer, S., Raabe, D., Friedel, F., Mattissen, D., 2015. Alloying effects on microstructure formation of dual phase steels. Acta Mater. 95, 386–398.

Shanthraj, P., Eisenlohr, P., Diehl, M., Roters, F., 2015. Numerically robust spectral methods for crystal plasticity simulations of heterogeneous materials. Int. J. Plast. 66, 31–45.

Shanthraj, P., Sharma, L., Svendsen, F., Roters, F., Raabe, D., 2016. A phase field model for damage in elasto-viscoplastic materials. Comput. Meth. Appl. Mech. Eng. 312, 167–185.

Shanthraj, P., Svendsen, F., Sharma, L., Roters, F., Raabe, D., 2017. Elasto-viscoplastic phase field modelling of anisotropic cleavage fracture. J. Mech. Phys. Solid. 99, 19–34.

Shinmiya, T., Ishikawa, N., Okatsu, M., Endo, S., Shikanai, N., Kondo, J., 2008. Development of high deformability linepipe with resistance to strain-aged hardening by heat treatment on-line process. Int. J. Offshore Polar Eng. 18, 308–313.

Steinmetz, D.R., Jäpel, T., Wietbrock, B., Eisenlohr, P., Gutierrez-Urrutia, I., Saeed-Akbari, A., Hickel, T., Roters, F., Raabe, D., 2013. Revealing the strain-hardening behavior of twinning-induced plasticity steels: theory, simulations, experiments. Acta Mater. 61, 494–510.

Takahashi, M., Sugiura, N., Ushigami, Y., Hara, T., Uemori, R., Shirahata, H., Mioguchi, M., Uenishi, A., Kojima, K., 2012. Metallurgical approaches for product development and process optimization. Nippon Steel Tech. Rep. 101, 128–137.

Tasan, C.C., Hoefnagels, J.P.M., Geers, M.G.D., 2010. Microstructural banding effects clarified through micrographic digital image correlation. Scripta Mater. 62, 835–838.

Tasan, C.C., Diehl, M., Yan, D., Zambaldi, C., Shanthraj, P., Roters, F., Raabe, D., 2014a. Integrated experimental–simulation analysis of stress and strain partitioning in multiphase alloys. Acta Mater. 81, 386–400.

Tasan, C.C., Hoefnagels, J.P.M., Diehl, M., Yan, D., Roters, F., Raabe, D., 2014b. Strain localization and damage in dual phase steels investigated by coupled in-situ deformation experiments-crystal plasticity simulations. Int. J. Plast. 63, 198–210.

Tasan, C.C., Diehl, M., Yan, D., Bechtold, M., Roters, F., Schemmann, L., Zheng, C., Peranio, N., Ponge, D., Koyama, M., Tsuzaki, K., Raabe, D., 2015. An overview of dual-phase steels: advances in microstructure-oriented processing and micromechanically guided design. Annu. Rev. Mater. Res. 45, 19.1–19.41.

Tsuyama, S., Nakamichi, H., Yamada, K., Endo, S., 2013. Effects of distribution and the formation process of MA on deformation and toughness of high strength

linepipe steel. ISIJ Int. 53, 317–322.

Wang, X., Pan, Z., Fan, F., Wang, J., Liu, Y., Mao, S.X., Zhu, T., Xia, S., 2015. Nanoscale deformation analysis with high-resolution transmission electron microscopy and digital image correlation. J. Appl. Mech. 82, 121001.

Wong, S.L., Madivala, M., Prahl, U., Roters, F., Raabe, D., 2016. A crystal plasticity model for twinning and transformation-induced plasticity. Acta Mater. 118, 140–151.

Yan, D., Tasan, C.C., Raabe, D., 2015. High resolution in situ mapping of microstrain and microstructure evolution reveals damage resistance criteria in dual phase steels. Acta Mater. 96, 399–409.

Zambaldi, C., Yang, Y., Bieler, T.R., Raabe, D., 2012. Orientation informed nanoindentation of alpha-titanium: indentation pileup in hexagonal metals deforming by prismatic slip. J. Mater. Res. 27 (1), 356–367.

Zhang, T., Jiang, J., Britton, B., Shollock, B., Dunne, F., 2016. Crack nucleation using combined crystal plasticity modelling, high-resolution digital image correlation and high-resolution electron backscatter diffraction in a superalloy containing non-metallic inclusions under fatigue. Proc. Roy. Soc. Lond. 472, 2189–2214.

Zhao, Z., Ramesh, M., Raabe, D., Cuitiño, A.M., Radovitzky, R., 2008. Investigation of three-dimensional aspects of grain-scale plastic surface deformation of an aluminum oligocrystal. Int. J. Plast. 24, 2278–2297.

Zhou, J., Horsley, D., Rothwell, B., 2006. Application of strain-based design for pipelines in permafrost areas. In: Proc. Of the 6th Int. Pipeline Conf. ASME, New York, pp. 899–907.